

# Coexistence of Quantum-Spin-Hall and Quantum-Hall-Topological-Insulating States in Graphene/hBN on SrTiO<sub>3</sub> Substrate

Reiji Obata, Mioko Kosugi, Takashi Kikkawa, Kazuyuki Kuroyama, Tomoyuki Yokouchi, Yuki Shiomi, Shigeo Maruyama, Kazuhiko Hirakawa, Eiji Saitoh, and Junji Haruyama\*

SrTiO<sub>3</sub> (STO) substrate, a perovskite oxide material known for its high dielectric constant ( $\epsilon$ ), facilitates the observation of various (high-temperature) quantum phenomena. A quantum Hall topological insulating (QHTI) state, comprising two copies of QH states with antiparallel two ferromagnetic edge-spin overlap protected by the U(1) axial rotation symmetry of spin polarization, has recently been achieved in low magnetic field ( $B$ ) even as high as  $\approx 100$  K in a monolayer graphene/thin hexagonal boron nitride (hBN) spacer placed on an STO substrate, thanks to the high  $\epsilon$  of STO. Despite the use of the heavy STO substrate, however, proximity-induced quantum spin Hall (QSH) states in 2D TI phases, featuring a topologically protected helical edge spin phase within time-reversal-symmetry, is not confirmed. Here, with the use of a monolayer hBN spacer, it is revealed the coexistence of QSH (at  $B = 0$  T) and QHTI (at  $B \neq 0$ ) states in the same single graphene sample placed on an STO, with a crossover regime between the two at low  $B$ . It is also classified that the different symmetries of the two nontrivial helical edge spin phases in the two states lead to different interaction with electron-puddle quantum dots, caused by a local surface pocket of the STO, in the crossover regime, resulting in a spin dephasing only for the QHTI state. The results obtained using STO substrates open the doors to investigations of novel QH spin states with different symmetries and their correlations with quantum phenomena. This exploration holds value for potential applications in spintronic devices.

## 1. Introduction

SrTiO<sub>3</sub> (STO) is a perovskite oxide material known for its high dielectric constant (e.g.,  $\epsilon \approx 10^4$  at temperature ( $T$ ) = 2 K). Because the STO causes no transition to a ferroelectric phase thanks to significant quantum fluctuations even at low  $T$  (i.e., quantum paraelectric phases), it holds a considerable advantage that high  $\epsilon$  leading to high carrier densities ( $n_D$ ) can be gate-controlled across all  $T$  regimes.<sup>[1–4]</sup> This gate-controlled property has enabled the observation of various (high- $T$ ) quantum phenomena (Supporting information S1),<sup>[5–10]</sup> such as high- $T_c$  ( $> 100$  K) superconductivity of atom-thin FeSe/STO arising from specific electronic states at the interface between the STO surface and directly grown layers,<sup>[5]</sup> high- $T_c$  ( $> 100$  K) Majorana fermion of Fe(Te, Se)/STO confirmed through scanning tunneling spectroscopy (STS).<sup>[6]</sup> Recently, a novel state of QH phases, a back-gate voltage ( $V_{bg}$ )-controlled quantum Hall topological insulating (TI) (QHTI) state (Figure 1a), has been reported by confirming the unconventional resistance ( $R$ )

R. Obata, M. Kosugi, J. Haruyama  
 Faculty of Science and Engineering  
 Aoyama Gakuin University  
 5-10-1 Fuchinobe, Sagamihara, Kanagawa 252-5258, Japan  
 E-mail: [J-haru@ee.aoyama.ac.jp](mailto:J-haru@ee.aoyama.ac.jp)  
 T. Kikkawa, E. Saitoh  
 Department of Applied Physics  
 The University of Tokyo  
 7-3-1 Hongo, Bunkyo-ku, Tokyo 113-8656, Japan  
 K. Kuroyama, K. Hirakawa, J. Haruyama  
 Institute for Industrial Sciences  
 The University of Tokyo  
 4-6-1 Komaba Meguro-ku, Tokyo 153-8505, Japan

T. Yokouchi, Y. Shiomi  
 Department of Basic Science  
 The University of Tokyo  
 3-6-1 Komaba Meguro-ku, Tokyo 153-8902, Japan  
 S. Maruyama  
 Department of Mechanical Engineering  
 The University of Tokyo  
 7-3-1 Hongo, Bunkyo-ku, Tokyo 113-8656, Japan  
 E. Saitoh  
 Institute for AI and Beyond  
 The University of Tokyo  
 7-3-1 Hongo, Bunkyo-ku, Tokyo 113-8656, Japan  
 E. Saitoh  
 WPI Advanced Institute for Materials Research  
 Tohoku University  
 2-1-1 Katahira, Aoba-ku, Sendai 980-8577, Japan  
 E. Saitoh  
 Advanced Science Research Center  
 Japan Atomic Energy Agency  
 2-4 Shirakata, Tokai-mura, Naka-gun, Ibaraki 319-1195, Japan

 The ORCID identification number(s) for the author(s) of this article can be found under <https://doi.org/10.1002/adma.202311339>

DOI: 10.1002/adma.202311339

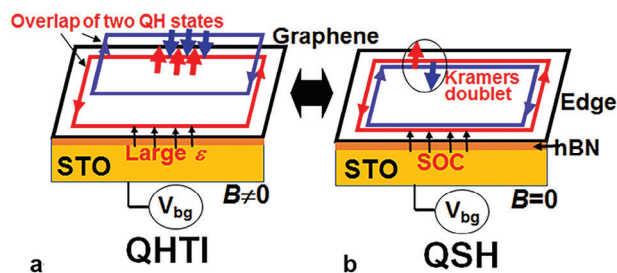


**Figure 1.** Schematic views of QHTI and QSH states in graphene/hBN/STO substrate. a) QHTI state; two copies of QH states with antiparallel spin overlap, forming two FM edge spin alignments. Short-range and lattice-scale AFM edge-spin alignment, enhanced by long-range CI exists in graphene. The large  $\epsilon$  of the STO induced by  $V_{bg}$  screens this CI, suppressing the AFM edge spins and possibly giving rise to the QHTI state. b) QSH state and its helical edge spin phases (i.e., Kramers doublet with AFM spin moment) derived from the SOC of the heavy STO substrate. Monolayer hBN spacer allows coexistence of a) and b). Both edge spin states in a) and b) appear analogous and nontrivial, though they consist of different symmetries; i.e., U(1) axial rotation symmetry of the spin polarization for a) and the topologically protected TRS for b). TRS is broken in a) through applied  $B$ . Only a) interacts with electron puddle quantum dots, leading to spin dephasing in the present experiments.

values associated with resistance quantum  $R_Q$  ( $= h/e^2 = 25.8$  k $\Omega$ , where  $h$  is Planck's constant, and  $e$  is the charge on the electron) under applied low magnetic fields ( $B$ ) even as high as  $T \approx 100$  K in monolayer graphene/thin hexagonal boron nitride (hBN) spacer (thickness  $\approx 2$ –5 nm) placed on an STO substrate.<sup>[7,11]</sup> A QHTI state is composed of two copies of QH states with an antiparallel spin overlap between the two ferromagnetic (FM) edge spin alignments (Figure 1a), which represents many-body interacting Landau level (LL)-induced TIs with a zero Chern number.<sup>[12,13]</sup>

Previously, the QHTIs in monolayer graphene on silicon (Si) substrates were reported only under the presence of a very strong in-plane  $B$  ( $> 30$  T)<sup>[12]</sup> or in misaligned graphene bilayers.<sup>[13]</sup> However, these approaches faced challenges due to the impractically strong and tilted  $B$  or the complexity of the twisted layer assembly. In contrast, the graphene/STO system offers significant advantages in terms of ease of fabrication and the application of low  $B$ , avoiding the difficulties encountered in previous methods and enabling the current research.<sup>[7]</sup> The screening of the long-range Coulomb interaction (CI) in graphene achieved through the  $V_{bg}$ -tuned large  $\epsilon$  of the STO substrate and subsequently caused the high  $n_D$  possibly allow this as explained later. As another case, the use of a ferrimagnetic insulator substrate,  $Y_3Fe_5O_{12}$ , has been also shown to induce ferromagnetic edge states in graphene.<sup>[39]</sup>

In contrast, despite the utilization of a heavy STO substrate, which provides strong spin–orbit coupling (SOC) for proximity-induced Quantum Spin Hall (QSH) states<sup>[7]</sup> (Figure 1b), the QSH state in the 2D Topological Insulator (TI) state was not observed, even at  $B = 0$  T, in the graphene/thin hexagonal boron nitride (hBN)/STO system. 2D TI states have been a subject of significant attention, featuring a topological bulk gap  $\Delta$  arising from SOC, while closing at sample edges. At  $B = 0$  T, the QSH state emerges with a resistance quantum  $R_Q/2$  value

and exhibits helical edge spin phases that are topologically protected by time-reversal symmetry (TRS). These states are characterized by nontrivial edge states with opposite-moment and counter-propagating spin pairs (i.e., Kramers doublets) flowing along 1D edges<sup>[14,15]</sup> (Figure 1b). QSH states have been previously reported in various materials, e.g., semiconductor quantum wells,<sup>[16–18]</sup> graphene,<sup>[19–26]</sup> and atomically thin transition metal dichalcogenides (TMDCs).<sup>[27–32]</sup> Notably, the relatively weak SOC in graphene has limited its experimental observation, with successful demonstrations in only a few systems, e.g., low-coverage  $Bi_2Te_3$  nanoparticle-decorated graphene<sup>[20,22,23]</sup> and graphene placed on heavy substrates with proximity-induced SOC (Figure 1b).<sup>[24–26]</sup>

In this context, the antiparallel spin overlaps between the two ferromagnetic (FM) edge spin states in the QHTI states (Figure 1a) and the helical edge spin states in the QSH states (Figure 1b) may appear analogous. However, a crucial distinction lies in the TRS. In the QHTI state, TRS is broken due to the presence of a finite applied  $B$ , unlike the QSH states where TRS is maintained in the helical edge states at  $B = 0$  T. Nevertheless, the U(1) axial rotation symmetry of the spin polarization remains continuous in the QHTI states, ensuring the persistence of nontrivial edge states.<sup>[7,11]</sup> This continuity in the U(1) axial rotation symmetry contributes to the observation of various  $R_Q$ -based (fractional) values, depending on the number and combination of ballistic charge transport regions separated by electrode probes, resembling the behavior in QSH states with spin dephasing in metal electrodes following the Landauer–Büttiker (LB) formalism.<sup>[27–29]</sup>

These two QH states are expected to be observed in one same graphene/STO sample, depending on  $B$ . However, previous attempts failed to observe them simultaneously. One possible cause could be the use of a thin hBN spacer ( $> \approx 3$  nm), which significantly suppresses proximity effect arising from SOC of the STO substrate.<sup>[4]</sup> To address this, we employ a monolayer hBN spacer in the present experiments, and classify that the QHTI and QSH states coexist with changes in  $B$  and  $V_{bg}$  in the same single sample. As mentioned above, these two QH states exhibit different symmetries in the helical edge spin phases. Understanding how these differences lead to varied interactions with physical phenomena is a fascinating aspect of our investigation. We reveal that only the helical edge spin phase of the QHTI state interacts with electron puddle quantum dots locating close to the edges, resulting in spin dephasing similar to the behavior observed for metal electrodes placed on the helical edge spin path, whereas the helical edge spin states in the QSH states remain robust under similar conditions.

## 2. Results and Discussion

### 2.1. Sample Fabrication

For the present experiments, monolayer graphene flakes ( $\approx 0.75$  nm thickness) mechanically exfoliated from bulk graphite (hq Graphene Co.) were carefully transferred onto a monolayer hBN/STO substrate (SHINKOSHA) (Figure 2a,b). In this process, a monolayer hBN was detached from the Cu foil and placed on the [100] plane of the nondoped STO substrate (refer the Experimental Section and Supporting Information S2).<sup>[4,10]</sup> Typical

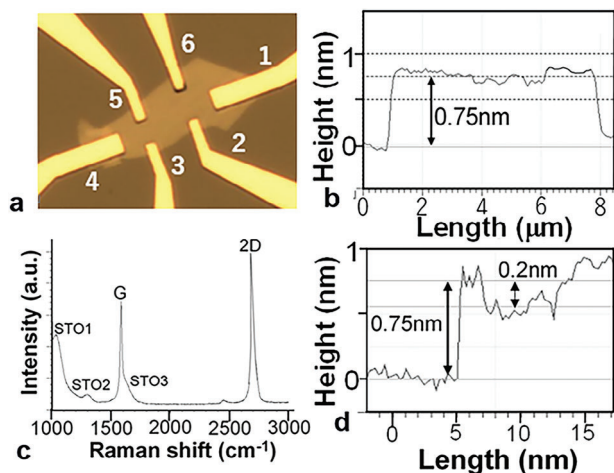


**Figure 2.** Sample characterization (Supporting Information S2 and S3). a) Optical microscopy image of a monolayer graphene flake on monolayer hBN spacer/STO substrate with Au/Ti (500/20 nm thickness) Hall-pattern electrodes. Each probe number corresponds to the respective  $R$  measurement. b) Cross-sectional AFMS image of graphene in a). c) A typical Raman spectrum of a). Individual peaks correspond to G and 2D ( $G'$ ) peaks of a monolayer graphene, as well as STO-originated peaks at approximately 1000 (STO1), 1300 (STO2), and 1600 (STO3)  $\text{cm}^{-1}$  (overlapping with the bottom of the graphene G peak). The hBN peak cannot be confirmed due to the overlap with G and STO3 peaks. d) An example of a cross-sectional AFMS image around the edge between electrodes 2 and 3 of a), corresponding to the position ① of Figure 4b; and Supporting Information S5.

Raman spectra are depicted in Figure 2c. The peaks at  $\approx 1600$  and  $2600 \text{ cm}^{-1}$  correspond to the G and 2D peaks of graphene, respectively. The peak ratio and width suggest the presence of monolayer graphene. The small peaks at  $\approx 1000$ ,  $1300$ , and  $1600 \text{ cm}^{-1}$  (overlapping the bottom of the G peak of graphene) are consistent with those of the STO substrate.<sup>[33]</sup> In contrast, the peak originating from the monolayer hBN overlaps with the G peak of graphene and the peak of STO cannot be confirmed, despite the certainty that the monolayer hBN was successfully transferred from the Cu foil, as mentioned above. Carrier density ( $n_{2D}$ )  $\approx 1 \times 10^{13} \text{ cm}^{-2}$ , electron mobility ( $\mu$ )  $\approx 5000 \text{ cm}^2 \text{ V}^{-1} \text{ s}^{-1}$ , and SOC energy ( $E_{\text{SOC}}$ )  $\approx 10 \text{ meV}$  of the graphene are estimated from other measurements conducted on larger graphene samples within a diffusive charge transport regime (Supporting Information S3). These  $E_{\text{SOC}}$  and  $n_{2D}$  values are large enough to yield the QSH state through the proximity effect and the QHTI state by the screening of long-range CI, which arise from the STO substrate, respectively, as explained later. Figure 2d presents an atomic-force microscope (AFMS) cross-sectional image around the edge between electrodes 2 and 3 of (a), corresponding to the position ① in Figure 4b; and Supporting Information S5. The local surface pocket, observed close proximity to the edge and resulting from the surface roughness of the STO substrate (Supporting Information S2), may give rise to an electron puddle quantum dot. This quantum dot manifests as a small  $dI/dV$  peak at the position ① in Figure 4b and serves as a basis of the model presented in Figure 5.

A Hall pattern, comprising six Au/Ti electrodes (500/200 nm thickness), was formed on graphene flakes through conventional

electron beam lithography (Figure 2a; and Supporting Information S4). Two-terminal resistance ( $R$ ) measurements, dependent on  $T$  and out-of-plane  $B$ , were conducted using DynaCool (Quantum Design) with a lock-in amplifier. The  $V_{\text{bg}}$  was applied from the back side of the STO substrate.

## 2.2. Resistance Measurements

Figure 3a presents an example of two-terminal resistance ( $R$ ) measurement results for Sample 1 (depicted in Figure 2) under three different current ( $I$ ) flow and  $R$  detection (Figure 3e–g), each for constant  $B = 0 \text{ T}$  and  $T = 2 \text{ K}$  with the  $V_{\text{bg}}$  varied. Distinct  $R$  peaks are observed in the curves for  $R_{63} \approx 3R_Q/2$  (blue curve),  $R_{14} \approx R_Q$  (red curve), and  $R_{64} \approx 3/4R_Q$  (green curve) values, occurring around  $V_{\text{bg}} \approx 0\text{--}2 \text{ V}$ , corresponding to the Dirac point. These  $R$  peak values align with those reported in previous studies on QSH states. The results are also consistent with calculations based on Equation (1) using the LB formalism,<sup>[16,23,27,28]</sup> which indicates dephasing of the spin phase due to back-scattering in metal electrode probes placed on 1D edges. Hence, an edge section between the two probes can be considered as an ideal helical quantum conductor of  $R_Q$ , and the two-terminal  $R$  of the device arises from the parallel  $R$  of both edges. Each edge contributes to the sum of the contributions from individual helical edge sections, denoted as,  $N$  (Supporting Information S5).

$$R_{2t} = \frac{h}{e^2} \left( \frac{1}{N_L} + \frac{1}{N_R} \right)^{-1} \quad (1)$$

In Equation (1),  $N_L$  and  $N_R$  represent the numbers of helical conductor sections for the left (L) and right (R) edges, respectively, between the source and drain probes. For the  $R_{63}$  measurement,  $N_L$  and  $N_R$  are both 3, yielding  $R_{63}$  as  $3R_Q/2$ . In the case of the  $R_{14}$  measurement,  $N_L$  and  $N_R$  are both 2, resulting in  $R_{14}$  being  $R_Q$ . Finally, for the  $R_{64}$  measurement,  $N_L$  is 3 and  $N_R$  is 1, leading to  $R_{64}$  resulting in  $(4/3)^{-1}R_Q$ . These calculated values precisely match the observed  $R$ -peak values as mentioned above (Supporting Information S5).

Consequently, the most likely explanation for the observed  $R$  peaks is presence of the QSH states, which arise from the proximity-induced SOC by the heavy STO substrate. The  $E_{\text{SOC}}$  value of  $\approx 10 \text{ meV}$  estimated in Supporting Information S3 is sufficient large to yield this. Notably, these QSH states were not observed in previous studies that employed thin hBN spacers ( $\approx 3 \text{ nm}$ ).<sup>[7]</sup> This observation suggests the intriguing possibility that the monolayer hBN spacer may enable the proximity-induced SOC from the heavy STO substrate, leading to the emergence of QSH states within graphene.

In Figure 3b,  $B$  dependence for the  $R_{14}$  versus  $V_{\text{bg}}$  relationships is presented for a different sample (Sample 2) with the same terminal configuration (i.e., pattern (e)) as that corresponding to the red curve in Figure 3a. Notably, an  $R$  peak with  $R_{14} \approx R_Q$  is evident at  $V_{\text{bg}} \approx 4 \text{ V}$  under  $B = 0 \text{ T}$ , similar to the observation in Figure 3a, although the  $V_{\text{bg}}$  positions and the shapes for the  $R$  peaks are different (Supporting Information S6). This further supports the potential presence of the QSH state in this sample. The confirmation of the QSH state is additionally supported by STS spectra

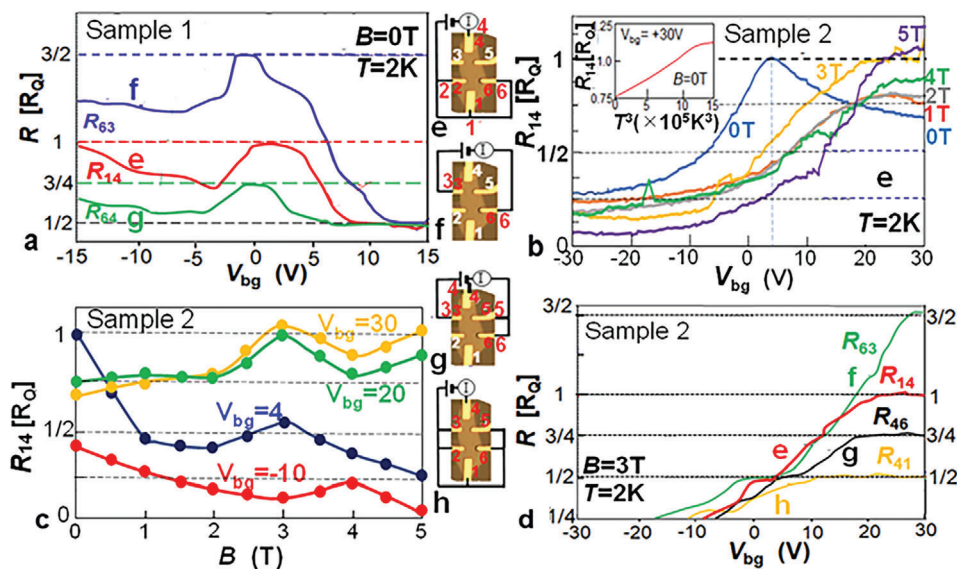


**Figure 3.** Two-terminal- $R$  measurements for QSH ( $B = 0$ ) and QHTI ( $B \neq 0$ ) states (Supporting Information S5). a)  $R$  measurement results as a function of  $V_{bg}$  for Sample 1. Three different configurations of electrode probes correspond to patterns (e–g), where red numbers indicate electrodes used for two-terminal  $R$  measurements, together with some probes. These curves represent the case for the QSH state observable at  $B = 0$  T. b)  $R_{14}$  versus  $V_{bg}$  relationships in Sample 2 (shown in Figure 2) for different perpendicular  $B$  values ( $= 0$ –5 T) to the sample plane. The probe configuration corresponds to e). Inset:  $T^3$  dependence of  $R_{62}$  at  $V_{bg} = +30$  V for  $B = 1$  T. c)  $R_{14}$  versus  $B$  relationships for individual  $V_{bg}$  obtained from b). d)  $R$  measurement results as a function of  $V_{bg}$  for four different configurations of electrode (probe) combinations e–h) at  $B = 3$  T in Figure 3b sample, including that of Figure 3b (i.e., red curve,  $R_{14}$ ).

in Section 2.3. The  $R$  peak value drastically decreases as  $B$  increases, experiencing a slight increase at  $B = 3$  T before sharply decreasing again toward  $B = 5$  T (Figure 3c).

In contrast,  $R$  plateaus appear in high  $V_{bg}$  regions as  $B$  increases (Figure 3b); i.e.,  $R_{14} \approx (3/4)R_Q$  at  $B = 1$  and 2 T,  $R_{14} \approx R_Q$  at  $B = 3$  and 5 T, with slightly reduced  $R_{14} \approx (4/5)R_Q$  at  $B = 4$  T for  $V_{bg} \approx +20 \approx +30$  V. The  $R$  versus  $B$  relationships for individual  $V_{bg}$  values in Figure 3c efficiently illustrate the behavior of  $R_{14}$  behavior at each  $V_{bg}$ , as mentioned above in Figure 3b. The  $R_{14}$  peak with  $R_Q$  at  $B = 3$  T does not persist at  $T = 100$  K (Supporting Information S7), contrary to a previous report.<sup>[7]</sup>

The observed  $R$  plateaus with  $R_{14} \approx R_Q$  observed under the application of  $B = 3$  and 5 T (Figure 3b) likely originate from causes different from the QSH states observable at  $B = 0$  T. Considering their appearance under  $B$ , one of the most probable scenarios is the QHTI state, as mentioned in the Introduction.<sup>[7,11]</sup> This interpretation is reaffirmed by Figure 3d, displaying  $R$  measurement results with four different configurations of electrode combinations (Figure 3e–h) at  $B = 3$  T, including that of Figure 3b. The observed  $R$  plateau values around  $V_{bg} \approx +20 \approx +30$  V (i.e.,  $R_{63} \approx 3/2R_Q$  (green curve),  $R_{14} \approx R_Q$  (red),  $R_{46} \approx 3/4R_Q$  (black), and  $R_{41} \approx R_Q/2$  (yellow curve)) align well with the calculation results using Equation (1), similar to the results in Figure 3a at  $B = 0$  T (Supporting Information S5). This strongly suggests that the  $R$  plateaus observed under applied  $B$  can be attributed to the QHTI state.

The edges of conventional graphene on Si substrate typically exhibit short-range, lattice-scale anti-FM (AFM) spin alignment, which hinders the emergence of 1D FM edge spin alignment and the QHTI state. The short-range AFM spin alignment may be en-

hanced by the long-range CI. Therefore, when the long-range CI is screened by the  $V_{bg}$ -tuned large  $\epsilon$  of the STO substrate and the high  $n_D$  in the graphene integrated on a monolayer hBN/STO substrate, the AFM edge spin alignment is suppressed. Subsequently, 1D FM edge spin alignment tends to appear, resulting in its antiparallel two overlap and the emergence of the QHTI states even at low  $B$ <sup>[7]</sup> (Figure 1a).

This result implies that the QSH and QHTI states can coexist in the same sample, with dependence on applied  $B$  when a monolayer hBN spacer is used. It suggests that both the proximity-induced SOC due to the heavy STO substrate at  $B = 0$  T and screening of the long-range CI due to the large  $\epsilon$  of the STO substrate at  $B \neq 0$  T can alter the electronic states of graphene in this case, while the SOC and the screening of the long-range CI have less influence on the QHTI at  $B \neq 0$  T and the QSH states  $B = 0$  T, respectively.

On the other hand,  $R$  plateaus with  $R_{14} \approx (3/4)R_Q$  values, occurring between  $B = 0$  T and 3 T (specifically at  $B = 1$  and 2 T in Figure 3b), are anomalous and have not been previously reported. According to previous report, a complete phase transition from the QSH to QHTI states should occur even at  $B = 1$  T. Therefore, these  $(3/4)R_Q$  values can be interpreted as occurring in a crossover regime between the QSH and QHTI states with a slight increase in  $B$ , and unique to the present samples.

### 2.3. STS Observation

To reconfirm the QSH state observed at  $B = 0$  T in Figure 3b, STS spectra have been obtained (Figure 4a; and Supporting

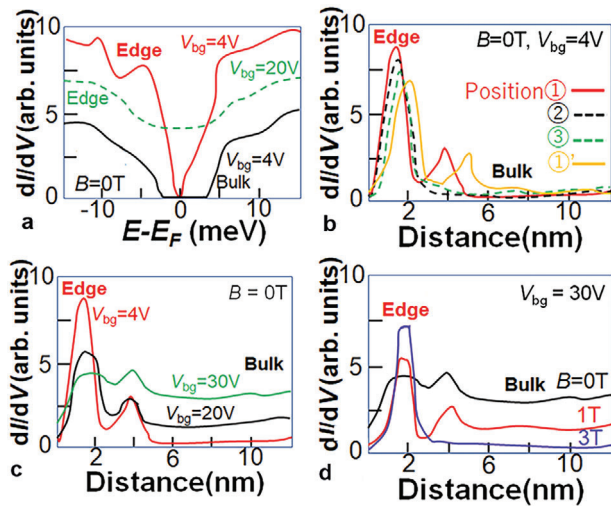


**Figure 4.** STS spectra for Figure 3b sample at  $T = 2$  K. a) At edge (red curve) and bulk (black curve) parts for  $V_{bg} = 4$  V, where  $E_F$  is tuned to the Dirac point, and at edge for different  $V_{bg} = 20$  V (green-dotted curve) with  $E_F$  far away from the Dirac point. b) Results of scanning STS tip from the edge to the bulk at four different positions between electrodes 2 and 3 (⊙ (related to Figure 2d) – ⊙), and 5 and 6 (⊙') (Figure S4 in Supporting Information S8), when  $E_F$  is tuned 5 meV away from the Dirac point. c)  $V_{bg}$  dependence at the position ⊙ in b). d)  $B$  dependence at  $V_{bg} = 30$  V in c).

Information S8). When the  $E_F$  is tuned close to Dirac point (i.e.,  $V_{bg} \approx 4$  V in Figure 3b), an energy gap  $\Delta \approx 5$  meV appears in the sample bulk region (black curve), while it closes at the sample edges (red curve). Conversely, when  $E_F$  is located away from Dirac point (i.e.,  $V_{bg} \approx 20$  V in Figure 3b),  $dI/dV$  increases over a wide  $E$  range. These results strongly support presence of the QSH state.

On the other hand, one of the causes for the observed  $R_{14} \approx (3/4)R_Q$  value at  $B = 1$  and 2 T in Figure 3b may be associated with the dephasing of the QHTI-derived helical edge states by the electron puddle quantum dots, which originates from the surface local-roughness of the STO substrate (Figure 2d),<sup>[4,10]</sup> observable through STS spectra (Figure 4b–d)<sup>[17,27,31,34,35]</sup> as follows.

Figure 4b exhibits results of scanning of the STS tip from the edge to the bulk at four different positions between electrodes 2 and 3 (⊙ – ⊙), and 5 and 6 (⊙') (Supporting Information S8). The presence of the small  $dI/dV$  peaks is confirmed near the large edge  $dI/dV$  peak (located  $\approx 4$ – $5$  nm away from the edge) only at the positions ⊙ and ⊙'. The large edge  $dI/dV$  peaks, observable when  $E_F$  is tuned slightly away from the Dirac point (Figure 4a), are sensitive to changes in  $V_{bg}$  (Figure 4b (as mentioned above) and 4c). Conversely, the small  $dI/dV$  peaks are not sensitive to  $V_{bg}$  and persist even at  $V_{bg} \approx 30$  V (Figure 4c). This suggests that the small  $dI/dV$  peaks are not associated with the QSH states. One possible cause for these small  $dI/dV$  peaks could be the presence of electron puddle quantum dots caused by the local surface pocket of the STO substrate (Figure 2d).<sup>[4,10]</sup>

Some reports claim that electron-puddle quantum dots, situated in close proximity to the helical edge states in the QSH states, can interact with them, leading to spin dephasing similar to the interaction in metal electrodes.<sup>[31,34,40]</sup> The linear relationship between  $R_{14}$  and  $T^3$  at  $B = 1$  T is confirmed up to  $T \approx 100$

K (inset of Figure 3b). This is qualitatively consistent with the theory proposing interaction-based dephasing,<sup>[34]</sup> although in the present case, it is not the QSH but the QHTI states that would interact with the electron-puddles at low  $B$ . As  $B$  increases further, the small  $dI/dV$  peak decreases and disappears around  $B = 3$  T, while another peak appears (Figure 4d).

## 2.4. Discussion

Based on our observations, we propose the following interpretation for the observed  $R_{14} \approx (3/4)R_Q$  value at  $B = 1$  and 2 T in Figure 3b, building upon Equation (1). When dephasing regions caused by electron puddles exist along both long edges of the sample (i.e., between Electrodes 2 and 3, and 5 and 6; refer positions ⊙ and ⊙' in Figure 4b), the number of helical conductor sections becomes three along individual edge paths (i.e.,  $N_L(3,2') = N_R(5,5',6) = 3$  Figure 5b). Moreover, considering that graphene exhibits an electron- and hole-like LL structure with a fourfold spin- and valley-degeneracy, if the number of helical edge spin paths appears in double (Figure 5),  $R_{14}$  can become  $(3/2)R_Q \times$

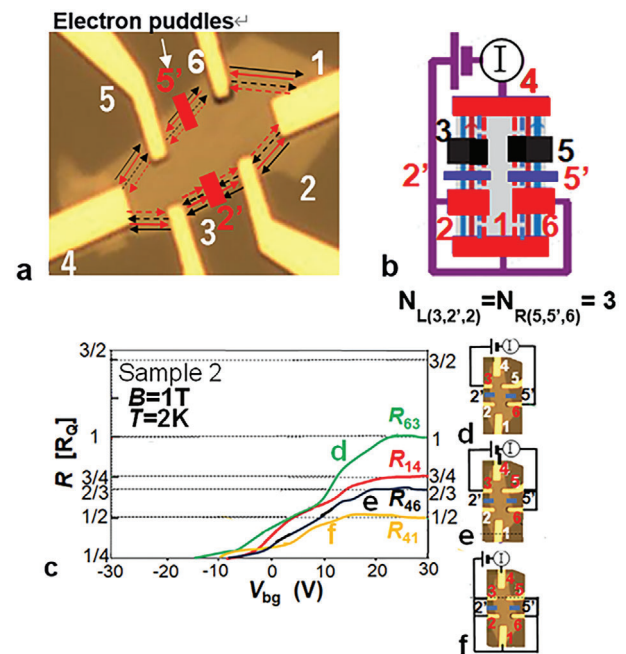


**Figure 5.** a) Schematic view for the electron-puddle spin dephasing model proposed for the crossover regimes between the QSH ( $B = 0$  T) and the QHTI ( $B \neq 0$  T) states (i.e.,  $R_{14} \approx (3/4)R_Q$  plateaus at  $B \approx 1$ – $2$  T in Figure 3b,c), which considers the interaction of the helical edge spins of the QHTI with the electron-puddle quantum dots caused by the local surface-pocket of the STO substrate (Figures 2d and 4b (⊙ and ⊙')) and assumes resolving of a fourfold spin- and valley-degeneracy (solid and dotted lines) by this interaction. The red parts (2' and 5') indicate local dephasing regions caused by the electron puddles. b) Schematic probe configuration corresponding to a).  $N_L$  and  $N_R$  correspond to the numbers of helical conductor (i.e., ballistic charge transport) sections for the left (L) and right (R) edges, respectively, between the source and drain probes (see Equation (1)). c)  $R$  measurement results as a function of  $V_{bg}$  at  $B = 1$  T (i.e., in the crossover regime) of Figure 3d sample for four different probe combinations d–f) and  $R_{14}$  of Figure 3d with 2' and 5' based on b) (Supporting Information S5).

$(1/2) = (3/4)R_Q$  (Supporting Information S5). When the strong interaction between the electron-puddle quantum dots and the helical edge states entirely resolves this degeneracy not only locally but across all regions of the helical edge path as  $B$  increases, lifting the spin degeneracy, the  $R_{14}$  of  $(3/4)R_Q$  value is obtained, as mentioned above.

Some studies reported that applying a bias voltage effectively injects spin-polarized carriers into TMDCs through various methods, leading to a population imbalance between  $\pm K$  valleys.<sup>[36,37]</sup> When such a strong valley imbalance occurs due to interaction with the electron puddles enhanced by the high  $\epsilon$  of the STO substrate likewise in this structure, the valley degeneracy can be resolved by the applied  $B$  and high  $\epsilon$ . This is particularly relevant as nontrivial helical edge states of the QHTI state are caused by the U(1) axial rotation symmetry of the spin polarization in the fourfold spin- and valley-degeneracy. The shift of  $V_{bg}$  positions for the  $R$  peak at  $B = 0$  T to higher  $V_{bg}$  values for the  $R$  plateaus under the influence of  $B$  might be associated with this interaction with electron puddles, resulting from the renormalization of the electronic density of states at Dirac point.

This model finds further support in Figure 5c, which presents the result at  $B = 1$  T, corresponding to Figure 3d-sample. The observed  $R$  plateaus in individual electrode combination (Figure 5d–f and  $R_{14}$  of Figure 3d with 2' and 5') exactly agrees with those estimated using the abovementioned model (Supporting Information S5).

As  $B$  increases further toward  $B = 3$  T, electron puddles are swept away due to the electron shift from bulk regions (i.e., depletion of electrons in the bulk) to the edges induced by applied  $B$  (Figure 4d). Then, conventional QHTI states appear with  $R_{14} \approx R_Q$  at  $B = 3$  T as the final state following the phase transition from the QSH to the QHTI states. The small deviation of  $R_{14}$  ( $\approx(4/5)R_Q$ ) (from  $R_Q$  values) at  $B = 4$  T may also be associated with other remaining small electron puddles, as it is known that electron puddles cause such small deviations.<sup>[12,31]</sup>

Consequently, Figure 3b can be interpreted as a result of a phase transition from the QSH states at  $B = 0$  T to the QHTI states at  $B \neq 0$  T, with a crossover regime caused by a slight increase in  $B$ . This transition occurs when the electron-puddle quantum dots exist and interact with the helical edge states with the U(1) axial rotation symmetry of the spin polarization in the QHTI states. Applying  $V_{bg} \approx +20 \approx +30$  V resulted in  $n_{2D}$  as high as  $\approx 10^{14}$  cm<sup>-2</sup> at  $T = 2$  K in TaS<sub>2</sub>/monolayer hBN/STO.<sup>[4]</sup> If this high  $n_{2D}$  value can also be achieved in the present graphene system, it would be capable of sufficiently screening the long-range CI. Indeed,  $n_{2D}$  as high as  $\approx 10^{13}$  cm<sup>-2</sup> at  $V_{bg} \approx 5$  V is confirmed by other measurements as mentioned above (Supporting Information S3). Since applying a higher  $V_{bg}$  induces further increases in  $n_{2D}$ , this screening is practically achievable. The use of a monolayer hBN spacer enables the observation of this phase transition.

In contrast, the absence of the QSH state has been confirmed when thin hBN spacers are employed, while the QHTI state is retained.<sup>[7]</sup> This implies that the proximity-induced SOC resulting from the STO substrate is more sensitive to the thickness of the hBN spacer than the formation of the high  $n_{2D}$  caused by the large  $\epsilon$  STO with applied  $V_{bg}$ . This interpretation is further supported in Supporting Information S9, where a bilayer hBN spacer has been employed.<sup>[38]</sup>

Remarkably, the crossover regime with spin dephasing caused by the electron puddle quantum dots at low  $B$  has been observed only for the QHTI state, while it did not appear for the QSH state at  $B = 0$  T, preserving the evident  $R_Q$ -value peaks dependent only on the measured electrode combinations. Similar behaviors have been confirmed in three samples, depending on the number and positions of the electron puddles. This result may present a contradiction to previous theoretical predictions,<sup>[34]</sup> although the materials and causes providing the QSH states are different from the present experiments (i.e., considering the intrinsic QSH state in the doped 2D semiconductor quantum wells,<sup>[34,40]</sup> while the proximity-effect from the STO substrate in graphene in the present case).

However, this intriguing phenomenon should depend on the correlation between the strength of the dephasing (i.e., inelastic backscattering) by electron puddles and the strength of the different symmetry of the QSH and QHTI states, each arising from different causes. If the strength follows the order “Symmetry of the QHTI state (arising from the high  $\epsilon$  of the STO) < Dephasing by puddles < Symmetry of the QSH state (originating from the large mass of the STO),” then only the QHTI state is dephased by the electron puddles in accordance with the following scenario.

Both the QSH and QHTI states have the nontrivial helical edge spin phases, while they exhibit different symmetries due to distinct causes as mentioned above; i.e., the QSH state possesses topologically protected TRS, whereas TRS is broken by an applied  $B$  in the QHTI state, preserving only the U(1) axial rotation symmetry of spin polarization. The realization of this QHTI symmetry typically requires specified conditions, i.e., applying extremely high  $B$ , usage of STO or YIG substrates. In the present case, the possible screening of the long-range CI in graphene by the high  $\epsilon$  of STO enhances the formation of this symmetry. However, presence of the electron puddles can easily impede this screening, leading to the dephasing of the helical edge spin path near the puddles. Moreover, when the electron puddles in graphene itself originate from the local surface roughness of the STO substrate (Figure 2d; and Supporting Information S2), this screening effect does not emerge around the puddle existing just above the roughness, causing the helical edge spins to disappear. Consequently, the symmetry of the QHTI state, in this context, is relatively weak.

On the other hand, the TRS in the QSH state is robust and strong, because the large mass of the STO substrate yielding the sturdy SOC is not affected by such local surface roughness of the STO, interfacing entirely with all areas of the graphene flakes. As reported in refs.<sup>[34]</sup> and,<sup>[40]</sup> stringent conditions for the electron puddle quantum dots must be satisfied to cause dephasing in this TRS in the helical edge currents; e.g., the high doping level of the puddles, the distance between the puddle and edge within an elastic width  $\Gamma \approx T$ , the energy spacing  $\delta$  in the dot  $\gg T$ , the strip width within the tunneling length (the electron penetration depth), and the long edge length (large puddle number). Unless the observed electron puddles meet all such conditions, dephasing cannot cause. Although it is difficult to straightforwardly compare this theory with the present results since the used materials are different as mentioned above, we estimate that  $\delta \gg T$  may be insufficient in our system as follows.

$\delta$  is given by  $\alpha^2 E_C$ , where  $\alpha = e^2/(\kappa h v)$  is the interaction parameter and  $E_C$  is the bandgap, and  $\kappa$  is the dielectric constant and  $v$  is the electron velocity. When  $\kappa \approx 4$  on hBN and  $v \approx 1.5$

$\times 10^8 \text{ cm s}^{-1}$  in graphene are employed,  $\alpha \approx 0.3$  is obtained. With using  $E_C \approx 5 \text{ meV}$  obtained from the present STS observation,  $\delta \approx 0.4 \text{ meV}$  is attained. This  $\delta$  value is not so large compared with the measured lowest  $T \approx 0.2 \text{ meV}$ . Consequently, the dephasing may be observed in much lower  $T$  region. Therefore, the TRS of the QSH phase is strong, and the abovementioned order for the symmetries can indeed hold.

This highlights the superior resilience of the helical edge spin phases in the QSH states against dephasing factors compared with the helical edge phases in QHTI states.

### 3. Conclusion

In conclusion, when graphene was placed on an STO substrate with a monolayer hBN spacer, we observed the quantized transport both at  $B = 0 \text{ T}$  and at  $B \neq 0 \text{ T}$  in the same graphene, depending on  $V_{bg}$ . Through evidencing presence of SOC, the former was interpreted as the helical edge spin states for a QSH phase with TRS, while the latter was interpreted as those for a QHTI phases with U(1) axial rotation symmetry of the spin polarization. The crossover  $B$ -regimes between the two states were also confirmed. The observed crossover region with a  $3/4R_Q$  plateau at low  $B$  was associated with dephasing of the helical edge spin states in the QHTI state, interacting with the electron-puddle quantum dots (i.e., potentially resolving of a fourfold spin- and valley-degeneracy) caused by the local surface pocket on the STO substrate edges. In contrast, the QSH phase remained unaffected by such electron puddles, and could be robust. This underscores the profound impact of the distinct symmetries of the two QH states on observable physical phenomena, particularly in terms of spin dephasing. Our findings pave the way for further exploration of novel QH spin states along graphene edges employing hBN/STO substrates, shedding light on symmetry-based phenomena and promising avenues for the development of innovative spintronic devices.

### 4. Experimental Section

*Fabrication of Graphene/Mono-(or Bi-)Layer hBN/STO Structure (Supporting Information S2 and S3):* Monolayer graphene flakes (hq Graphene Co.) were attached on monolayer hexagonal boron nitride (hBN) spacer/STO substrate (SHINKOSHA) with a thickness of 0.5 mm. Initially, monolayer hBN, grown on Cu film by CVD, was detached from the Cu film by dissolving Cu film through treatment with PMMA and immersion in FeCl solution for 24 h. Subsequently, the monolayer hBN/PMMA was positioned on the [100] plane of a nondoped STO substrate (SHINKOSHA: dielectric constant  $\approx 300$  at 300 K and  $\approx 10^4$  at 2 K, 0.5 mm thickness, purity  $> 99.98\%$ , resistivity  $> 10^7 \Omega \text{ cm}$ ) creating an interface STO and hBN. The surface-side PMMA was, then, dissolved in an acetone solution for a half day, resulting in the formation of the monolayer hBN/STO substrate. Finally, any remaining PMMA contamination on hBN was removed through  $\text{O}_2$  plasma treatment at  $300 \text{ }^\circ\text{C}$  for 30 min. The crystal quality of the hBN was subsequently verified by Raman spectroscopy (Supporting Information S2).

Monolayer graphene flakes were attached on this hBN/STO substrate from a PDMS sheet, using a 2D heterostructure transfer system (hq Graphene Co.). Initially, graphene flakes were mechanically exfoliated using the scotch tape method, and the resulting flakes were transferred from the tape surface to the PDMS sheet. Then, they were transferred onto the hBN/STO utilizing the 2D transfer system at  $300 \text{ }^\circ\text{C}$ . The STO substrates employed here have notable surface roughness at certain local

points (Figure 2A–C), which is anticipated to contribute to formation of electron puddle quantum dots (Figure 4B).

The monolayer graphene was characterized using Raman spectroscopy and AFMS.

*STS Measurements (Supporting Information S8):* STS measurements were carried out using UNISOKU USM series with a tip diameter of  $\approx 50 \text{ nm}$  by varying  $T$ ,  $V_{bg}$ , and  $B$  with scanning for  $\text{①}$ – $\text{③}$  and  $\text{④}$ . They were measured at points shown in Supporting Information S8 by using the standard lock-in technique.

### Supporting Information

Supporting Information is available from the Wiley Online Library or from the author.

### Acknowledgements

The authors gratefully acknowledged J. Sandeep, B. Skinner, K. Otsuka, J. Oka, S. Noda, S. Murakami, T. Yamamoto, S. Tarucha, T. Ando, T. Enoki, A. MacDonald, R. Wu, J. Alecia, and J. J. Palacios for their technical supports, fruitful discussions, and strong encouragement. This work performed at Aoyama Gakuin University was supported by the Aoyama Gakuin University Research Institute grant program for the creation of innovative research. Works at the University of Tokyo were partially supported by JSPS KAKENHI (Grant Numbers JP23H00174, JP23H05443 for S. M. and JP19H05600, JP22K18686, JP22H05114 for T. K. and E. S.) and by JST, CREST (Grant Numbers JRMJCR20B5 for S. M. and JPMJCR20C1 and JPMJCR20T2 for T. K. and E. S.), MEXT Initiative to Establish Next-generation Novel Integrated Circuits Centers (X-NICS) (JPJ011438), Japan and Institute for AI and Beyond of the University of Tokyo for T. K. and E. S.

### Conflict of Interest

The authors declare no conflict of interest.

### Data Availability Statement

The data that support the findings of this study are available in the Supporting Information of this article.

### Keywords

graphene, helical edge spin phase, quantum hall topological insulating state, quantum spin hall state, SrTiO<sub>3</sub> substrate

Received: October 28, 2023

Revised: January 30, 2024

Published online:

- [1] T. Sakudo, H. Unoki, *Phys. Rev. Lett.* **1971**, *26*, 851.
- [2] D. Shin, S. Latini, C. Schäfer, S. A. Sato, U. De Giovannini, H. Hübener, A. Rubio, *Phys. Rev. B* **2021**, *104*, L060103.
- [3] X. He, D. Bansal, B. Winn, S. Chi, L. Boatner, O. Delaire, *Phys. Rev. Lett.* **2020**, *124*, 145901.
- [4] M. Kosugi, R. Obata, K. Suzuki, K. Kuroyama, S. Du, B. Skinner, T. Kikkawa, T. Yokouchi, Y. Shiomi, S. Maruyama, K. Hirakawa, E. Saitoh, J. Haruyama, *APL Mater.* **2023**, *11*, 081106.
- [5] J.-F. Ge, Z.-L. Liu, C. Liu, C.-L. Gao, D. Qian, Q.-K. Xue, Y. Liu, J.-F. Jia, *Nat. Mater.* **2015**, *14*, 285.

- [6] C. Chen, K. Jiang, Y. Zhang, C. Liu, Y. Liu, Z. Wang, J. Wang, *Nat. Phys.* **2020**, *16*, 536.
- [7] L. Veyrat, C. Déprez, A. Coissard, X. Li, F. Gay, K. Watanabe, T. Taniguchi, Z. Han, B. A. Piot, H. Sellier, B. Sacépé, *Science* **2020**, *367*, 781.
- [8] A. K. Pedersen, S. Ichinokura, T. Tanaka, R. Shimizu, T. Hitosugi, T. Hirahara, *Phys. Rev. Lett.* **2020**, *124*, 227002.
- [9] S. Das, Y. L. Tang, Z. Hong, M. A. P. Gonçalves, M. R. McCarter, C. Klewe, K. X. Nguyen, F. Gómez-Ortiz, P. Shafer, E. Arenholz, V. A. Stoica, S.-L. Hsu, B. Wang, C. Ophus, J. F. Liu, C. T. Nelson, S. Saremi, B. Prasad, A. B. Mei, D. G. Schlom, J. Íñiguez, P. García-Fernández, D. A. Muller, L. Q. Chen, J. Junquera, L. W. Martin, R. Ramesh, *Nature* **2019**, *568*, 368.
- [10] W. Si, T. Tanaka, S. Ichinokura, T. Hirahara, *Phys. Rev. B* **2022**, *105*, 104502.
- [11] M. Kharitonov, S. Juergens, B. Trauzettel, *Phys. Rev. B* **2016**, *94*, 035146.
- [12] A. F. Young, J. D. Sanchez-Yamagishi, B. Hunt, S. H. Choi, K. Watanabe, T. Taniguchi, R. C. Ashoori, P. Jarillo-Herrero, *Nature* **2014**, *505*, 528.
- [13] J. D. Sanchez-Yamagishi, J. Y. Luo, A. F. Young, B. M. Hunt, K. Watanabe, T. Taniguchi, R. C. Ashoori, P. Jarillo-Herrero, *Nat. Nanotechnol.* **2017**, *12*, 118.
- [14] J. Haruyama, *J. Appl. Phys.* **2021**, *129*, 090902.
- [15] J. Haruyama, *Adv. Quantum Technol.* **2022**, *5*, 2100096.
- [16] A. Roth, C. Brüne, H. Buhmann, L. W. Molenkamp, J. Maciejko, X.-L. Qi, S.-C. Zhang, *Science* **2009**, *325*, 294.
- [17] C. Brüne, A. Roth, H. Buhmann, E. M. Hankiewicz, L. W. Molenkamp, J. Maciejko, X.-L. Qi, S.-C. Zhang, *Nat. Phys.* **2012**, *8*, 485.
- [18] L. Du, I. Knez, G. Sullivan, R.-R. Du, *Phys. Rev. Lett.* **2015**, *114*, 096802.
- [19] C. L. Kane, E. J. Mele, *Phys. Rev. Lett.* **2005**, *95*, 226801.
- [20] J. Hu, J. Alicea, R. Wu, M. Franz, *Phys. Rev. Lett.* **2012**, *109*, 266801.
- [21] H. Jiang, Z. Qiao, H. Liu, J. Shi, Q. Niu, *Phys. Rev. Lett.* **2012**, *109*, 116803.
- [22] T. Namba, K. Tamura, K. Hatsuda, T. Nakamura, C. Ohata, S. Katsumoto, J. Haruyama, *Appl. Phys. Lett.* **2018**, *113*, 053106.
- [23] K. Hatsuda, H. Mine, T. Nakamura, J. Li, R. Wu, S. Katsumoto, J. Haruyama, *Sci. Adv.* **2018**, *4*, eaau6915.
- [24] J. O. Island, X. Cui, C. Lewandowski, J. Y. Khoo, E. M. Spanton, H. Zhou, D. Rhodes, J. C. Hone, T. Taniguchi, K. Watanabe, L. S. Levitov, M. P. Zaletel, A. F. Young, *Nature* **2019**, *571*, 85.
- [25] P. Tiwari, S. K. Srivastav, A. Bid, *Phys. Rev. Lett.* **2021**, *126*, 096801.
- [26] T. Wakamura, F. Reale, P. Palczynski, S. Guéron, C. Mattevi, H. Bouchiat, *Phys. Rev. Lett.* **2018**, *120*, 106802.
- [27] H. Mine, A. Kobayashi, T. Nakamura, T. Inoue, S. Pakdel, D. Marian, E. Gonzalez-Marin, S. Maruyama, S. Katsumoto, A. Fortunelli, J. J. Palacios, J. Haruyama, *Phys. Rev. Lett.* **2019**, *123*, 146803.
- [28] N. Katsuragawa, M. Nishizawa, T. Nakamura, T. Inoue, S. Pakdel, S. Maruyama, S. Katsumoto, J. J. Palacios, J. Haruyama, *Commun. Mater.* **2020**, *1*, 51.
- [29] X. Qian, J. Liu, L. Fu, J. Li, *Science* **2014**, *346*, 1344.
- [30] Z. Fei, T. Palomaki, S. Wu, W. Zhao, X. Cai, B. Sun, P. Nguyen, J. Finney, X. Xu, D. H. Cobden, *Nat. Phys.* **2017**, *13*, 677.
- [31] S. Wu, V. Fatemi, Q. D. Gibson, K. Watanabe, T. Taniguchi, R. J. Cava, P. Jarillo-Herrero, *Science* **2018**, *359*, 76.
- [32] S. Tang, C. Zhang, D. Wong, Z. Pedramrazi, H.-Z. Tsai, C. Jia, B. Moritz, M. Claassen, H. Ryu, S. Kahn, J. Jiang, H. Yan, M. Hashimoto, D. Lu, R. G. Moore, C.-C. Hwang, C. Hwang, Z. Hussain, Y. Chen, M. M. Ugeda, Z. Liu, X. Xie, T. P. Devereaux, M. F. Crommie, S.-K. Mo, Z.-X. Shen, *Nat. Phys.* **2017**, *13*, 683.
- [33] S. Saha, O. Kahya, M. Jaiswal, A. Srivastava, A. Annadi, J. Balakrishnan, A. Pachoud, C.-T. Toh, B.-H. Hong, J.-H. Ahn, T. Venkatesan, B. Özyilmaz, *Sci. Rep.* **2014**, *4*, 6173.
- [34] J. I. Väyrynen, M. Goldstein, L. I. Glazman, *Phys. Rev. Lett.* **2013**, *110*, 216402.
- [35] M. König, M. Baenninger, A. G. F. Garcia, N. Harjee, B. L. Pruitt, C. Ames, P. Leubner, C. Brune, H. Buhmann, L. W. Molenkamp, D. G. Gordon, *Phys. Rev. X* **2013**, *3*, 021003.
- [36] J.-X. Li, W.-Q. Li, S.-H. Hung, P.-L. Chen, Y.-C. Yang, T.-Y. Chang, P.-W. Chiu, H.-T. Jeng, C.-H. Liu, *Nat. Nanotechnol.* **2022**, *17*, 721.
- [37] Y. Ye, J. Xiao, H. Wang, Z. Ye, H. Zhu, M. Zhao, Y. Wang, J. Zhao, X. Yin, X. Zhang, *Nat. Nanotechnol.* **2016**, *11*, 598.
- [38]  $R_{14} \approx (3/4)R_Q$  was not observed in ref. 7 using thin hBN spacers. This might be just attributed to the good surface flatness of the STO used in ref. [7]. Otherwise, this might imply that influence of the STO surface roughness is weak for electronic states of the graphene, when thicker hBN spacer is used.
- [39] Y. Li, et al., *Phys. Rev. B* **2020**, *101*, 241405(R).
- [40] L. Lunczer, P. Leubner, M. Endres, V. L. Müller, C. Brüne, H. Buhmann, L. W. Molenkamp, *Phys. Rev. Lett.* **2019**, *123*, 047701.